JGR Atmospheres

RESEARCH ARTICLE
10.1029/2021JD034933

All-Sky Aerosol Direct Radiative Effects at the ARM SGP Site

Kelly A. Balmes[1,2,3] **and Qiang Fu**[1]

[1]Department of Atmospheric Sciences, University of Washington, Seattle, WA, USA, [2]Cooperative Institute for Research in the Environmental Sciences, University of Colorado, Boulder, CO, USA, [3]NOAA Global Monitoring Laboratory, Boulder, CO, USA

Key Points:

- All-sky aerosol direct radiative effect (DRE) was estimated using multiyear ground-based observations at ARM Southern Great Plains site for the first time
- The annual mean all-sky aerosol DRE at the top of the atmosphere (TOA) is -2.13 ± 0.54 W m^{-2}, compared to -3.00 ± 0.58 W m^{-2} for clear-skies
- The relative uncertainty in estimated all-sky TOA aerosol DRE due to aerosol single-scattering albedo errors is larger than for clear-skies

Correspondence to:
K. A. Balmes,
kelly.balmes@noaa.gov

Citation:
Balmes, K. A., & Fu, Q. (2021). All-sky aerosol direct radiative effects at the ARM SGP site. *Journal of Geophysical Research: Atmospheres*, *126*, e2021JD034933. https://doi.org/10.1029/2021JD034933

Received 18 MAR 2021
Accepted 3 AUG 2021

Abstract All-sky aerosol direct radiative effect (DRE) was estimated for the first time at the Atmospheric Radiation Measurement Southern Great Plains site using multiyear ground-based observations. The NASA Langley Fu-Liou radiation model was employed. Observed inputs for the radiation model include aerosol and cloud vertical extinction profile from Raman lidar; spectral aerosol optical depth, single-scattering albedo, and asymmetry factor from Aerosol Robotic Network; cloud water content profiles from radars; temperature and water vapor profiles from radiosondes; and surface shortwave spectral albedo from radiometers. A cloudy-sky radiative closure experiment was performed. The relative mean differences between modeled and observed surface downwelling shortwave total fluxes were 6% (7%) for transparent (opaque) cloudy-skies. The estimated annual mean all-sky aerosol DRE is -2.13 ± 0.54 W m^{-2} at the top of atmosphere (TOA) and -5.95 ± 0.87 W m^{-2} at the surface, compared to -3.00 ± 0.58 W m^{-2} and -6.85 ± 1.00 W m^{-2}, respectively, under clear-sky conditions. The seasonal cycle of all-sky aerosol DRE is similar to that of the clear-sky, except with secondary influences of the clouds: The cloud radiative effect is strongest (most negative) in the spring, which reduces the all-sky aerosol DRE. The relative uncertainties in all-sky aerosol DRE due to measurement errors are generally comparable to those in clear-sky conditions except for the aerosol single-scattering albedo. The TOA all-sky aerosol DRE relative uncertainty due to aerosol single-scattering albedo uncertainty is larger than that in clear-sky, leading to a larger total relative uncertainty. The measurement errors in cloud properties have small effects on the all-sky aerosol DRE.

1. Introduction

Aerosols modify Earth's radiative energy budget directly via scattering and absorbing radiation, which is referred to as the aerosol direct radiative effect (DRE). The aerosol DRE is also referred to as the radiative effect due to aerosol-radiation interactions (RE_{ari}) in the Intergovernmental Panel on Climate Change (IPCC) report (Boucher et al., 2013). In order to quantify the aerosol DRE, knowledge of aerosol optical properties including aerosol optical depth (AOD), single-scattering albedo, and asymmetry factor, are required vertically and spectrally, along with the characterization of the surface properties, cloud optical properties, atmospheric state, and Sun-Earth geometry.

All-sky global-mean shortwave (SW) aerosol DRE estimates at the top of the atmosphere (TOA) are about -2 W m^{-2} (e.g., Henderson et al., 2013; Matus et al., 2015, 2019; Oikawa et al., 2018). Passive satellite remote sensing estimates of the aerosol DRE rely on column-averaged observations that are often limited to cloud-free ocean (Yu et al., 2006). Active sensors such as the Cloud-Aerosol Lidar and Infrared Pathfinder Satellite (CALIPSO) provides the opportunity to have vertical profiles of aerosol and clouds over both ocean and land, which allows for more comprehensive all-sky aerosol DRE global estimates. However, several studies have documented that optically thinner aerosol can go undetected by CALIPSO (Kacenelenbogen et al., 2014; Omar et al., 2013; Redemann et al., 2012; Rogers et al., 2014; Thorsen & Fu, 2015b). Thorsen and Fu (2015b) showed that CALIPSO does not detect all radiatively significant aerosols due to instrument sensitivity. Thorsen et al. (2017) further showed that the undetected aerosols result in an underestimate of the global mean AOD, which ultimately leads to an underestimate in the global mean aerosol DRE of up to ~50%.

Ground-based observations provide the opportunity to make regional estimates of the aerosol DRE (e.g., Bansal et al., 2019; Che et al., 2019; Di Biagio et al., 2009, 2010; Mortier et al., 2016; Sherman & McComiskey, 2018; Xia et al., 2016). Regional estimates can then be useful to compare and validate satellite estimates. The high-quality ground-based observations at the Atmospheric Radiation Measurement Program (ARM) sites (Ackerman & Stokes, 2003) provide the opportunity to utilize observations of aerosol, cloud, radiation, and the atmospheric state to quantify the aerosol DRE. Previous studies have quantified the clear-sky aerosol DRE at the ARM sites (e.g., Creekmore et al., 2014; Delene & Ogren, 2002; Fu et al., 1999; Iziomon & Lohmann, 2003; Michalsky et al., 2006; Wu et al., 2021). However, no study to date has quantified the all-sky aerosol DRE at the ARM sites based on ground-based observations.

In Wu et al. (2021), we quantified the clear-sky aerosol DRE at the ARM Southern Great Plains (SGP) and Tropical Western Pacific (TWP) sites using multiyear ground-based observations. Herein, we quantify the all-sky aerosol DRE by considering the aerosol DRE for both cloudy-skies and clear-skies at the ARM SGP site. Note that we do not consider the ARM TWP site in this study as we did in Wu et al. (2021) due to the limited data availability hampering the ability to estimate the cloudy-sky aerosol DRE.

By inputting the ground-based observations into the NASA Langley Fu-Liou radiative transfer (RT) model (Fu, 1996; Fu & Liou, 1992, 1993; Fu et al., 1998; Rose et al., 2006; Rose & Charlock, 2002), the regional aerosol DRE can be estimated by quantifying how the radiative fluxes change in an atmosphere with and without aerosols. As in Wu et al. (2021), the ground-based Raman lidars (RL; Ferrare et al., 2006; Goldsmith et al., 1998; Newsom, 2009) are utilized for aerosol vertical detection and extinction profile (Balmes & Fu, 2018; Balmes et al., 2019; Thorsen & Fu, 2015a, 2015b; Thorsen et al., 2015, 2017) while the Aerosol Robotic Network (AERONET) Cimel sun photometers provide AOD, single-scattering albedo, and asymmetry factor at several wavelengths (Giles et al., 2019; Holben et al., 1998). To estimate the aerosol DRE under cloudy-skies, the RL cloud vertical detection and extinction profiles are utilized. In addition, the Active Remote Sensing of Clouds (ARSCLs) value-added product (Clothiaux et al., 2001) from the Ka-band Zenith ARM radar (KAZR) and the millimeter cloud radar (MMCR) supplements the RL observations to provide cloud and precipitation observations when the lidar becomes fully attenuated. The all-sky aerosol DRE is then quantified in terms of the daily mean, monthly mean, seasonal cycle, and annual-mean climatology.

Section 2 describes the aerosol and cloud optical properties from the RL, KAZR, and MMCR, as well as the RT model and other observational data employed in this study. Section 3 presents the radiative closure experiment under cloudy-sky conditions by comparing simulated surface downwelling SW fluxes using observed inputs with the corresponding observed fluxes. Section 4 presents the daily mean as well as the seasonal cycle of the all-sky aerosol DREs. Section 5 quantifies the measurement uncertainties for the estimated all-sky aerosol DREs. Section 6 summarizes and presents concluding remarks.

2. Data and Radiation Model

2.1. Aerosol and Cloud Profiles

2.1.1. ARM RL

The ARM Raman lidar (RL; Ferrare et al., 2006; Goldsmith et al., 1998; Newsom, 2009) provides vertical profiles of retrieved aerosol and cloud extinction at 355 nm from the feature detection and extinction (RL-FEX) retrieval algorithm (Balmes & Fu, 2018; Balmes et al., 2019; Thorsen & Fu, 2015a; Thorsen et al., 2015, 2017; Wu et al., 2021). In this study, a temporal resolution of 10 min and a vertical resolution of 30 m are considered from August 1, 2008 to August 31, 2016 at the SGP site in Lamont, Oklahoma (36.61°N, 97.49°W). Profiles in which the lidar beam does not fully attenuate are referred to as transparent profiles, which are those when the signal-to-noise ratio is greater than 1 at 16 km (Balmes et al., 2019; Thorsen et al., 2015).

Figures 1a and 1b show an example of feature classification and extinction coefficient from the RL, respectively, as a function of time and height retrieved on January 28, 2013 over the ARM SGP site. On this day, there are periods of clear-skies until around 12 UTC and then cloudy-skies after that. Ice clouds are present around 10–12 km and liquid clouds are present around 0.5–2.5 km after around 16 UTC. From 12 to 18

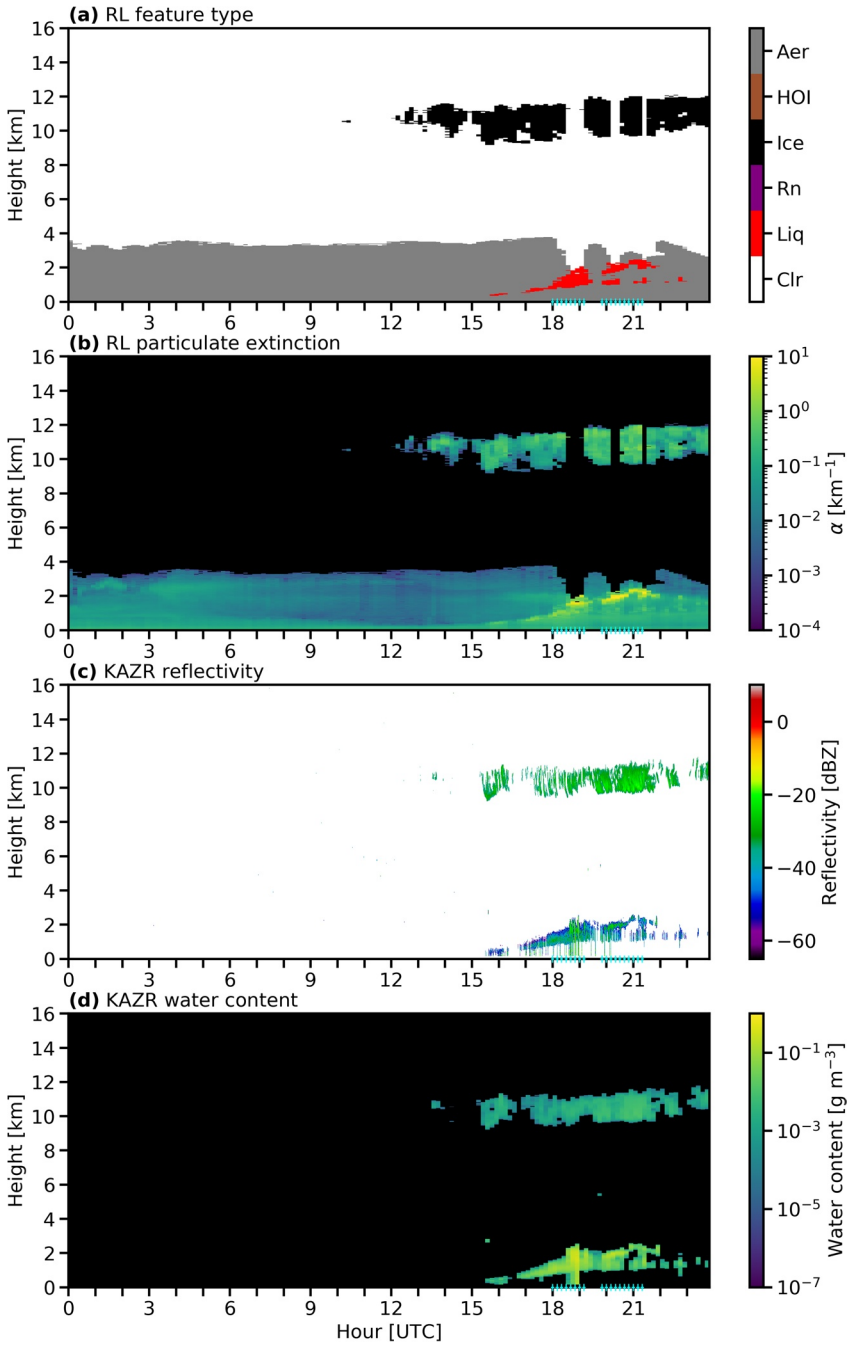

Figure 1. Raman lidar (RL) and Ka-band ARM Zenith Radar (KAZR) observations on January 28, 2013 at the Southern Great Plains (SGP) site. (a) RL feature type as liquid cloud (red), rain (purple), horizontally oriented ice (HOI; brown), ice cloud (black), or aerosol (gray). (b) RL feature particulate extinction (α; km^{-1}) at 355 nm. (c) KAZR reflectivity (dBZ). (d) KAZR-retrieved hydrometeor water content (g m^{-3}). The light blue "+" along the *x*-axis indicates the periods when the RL became fully attenuated.

UTC and then again after 21 UTC, the cloudy-sky profiles are transparent to the RL, which we refer to as transparent cloudy-sky. There are a few intervals of cloudy-sky periods during 18–21 UTC when the RL fully attenuates, which are referred to as opaque cloudy-sky.

The occurrence fraction of clear-sky, transparent cloudy-sky, and opaque cloudy-sky for the entire 8 yr time period at SGP is presented in Figure 2. The clear-sky fraction is 0.38 and the cloud fraction is 0.62. The cloud

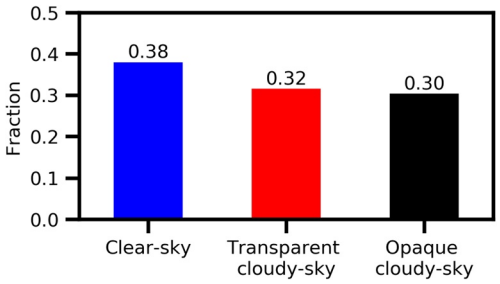

Figure 2. Clear-sky (left) and cloud fractions for the Raman lidar (RL) at the Southern Great Plains (SGP) site from August 2008 to August 2016. The cloud fraction is partitioned into those transparent (middle) and opaque (right) to the RL. The fraction is labeled above each bar.

fraction is further separated into transparent and opaque cloudy-sky as described above, which correspond to 0.32 and 0.30, respectively.

In this study, RL aerosol and cloud extinction profiles are used for clear-sky and transparent cloudy-sky profiles. For the aerosol profiles in opaque cloudy-sky conditions, the RL aerosol extinction profile below the level where the RL signal becomes fully attenuated is utilized. For the atmosphere above the RL attenuated level, the weekly mean cloudy-sky aerosol extinction profile is used at levels where the radar did not detect clouds or precipitation and cloud liquid and ice water profiles are based on the radar retrievals as described next.

In addition to the RL extinction profile for transparent cloudy-sky profiles, the cloud particle size is also needed as input to the radiative transfer model (Section 2.2). The liquid cloud effective radius is set as 6.54 microns for transparent cloudy-sky profiles, which is used in multiple retrieval algorithms (Zhao et al., 2012) as well as in the RL retrieval algorithm (Thorsen & Fu, 2015a). The ice cloud effective diameter is derived as a function of temperature following Heymsfield et al. (2014).

2.1.2. Radar Retrievals

For opaque cloudy-sky profiles in which the RL fully attenuated, the ARSCLs value-added product (Clothiaux et al., 2001) is used to retrieve cloud properties. ARSCL from the MMCR is used for August 2008 to January 2011 and from the KAZR for January 2011 to August 2016. The temporal resolution is 10 s and the vertical resolution is 43 m for the MMCR and 4 s and 30 m for the KAZR. The cloud retrievals are adapted from those used in Thorsen et al. (2013) and the ARM value-added products MICROBASE (Dunn et al., 2011) and CombRet (Comstock et al., 2013). The cloud layer boundaries, reflectivity, and temperature are used to retrieve cloud water content with the phase determined by temperature following MICROBASE (Dunn et al., 2011).

For liquid clouds, the liquid water content (LWC) is retrieved from reflectivity following Liao and Sassen (1994) with the cloud particle number concentration set as 100 cm^{-3} Dunn et al., 2011). For opaque cloudy-sky profiles, the liquid cloud effective radius is retrieved from the LWC following Dunn et al. (2011) and Frisch et al. (1995) with the assumption of a log-normal droplet distribution with a width of 0.35. In contrast to Dunn et al. (2011), the cloud particle number concentration is set as 100 cm^{-3} following Thorsen et al. (2013).

For ice clouds, the ice water content (IWC) is retrieved from temperature and reflectivity following Hogan et al. (2006). In the same manner, as transparent cloudy-sky (Section 2.1.1), the opaque cloudy-sky ice cloud effective diameter is from Heymsfield et al. (2014).

When the reflectivity is greater than −7 dBZ with temperature greater than 0 °C (Fueglistaler & Fu, 2006), we consider the reflectivity to be due to liquid precipitation. The rain water content (RWC) is retrieved from the reflectivity following Wood (2005). After the LWC is retrieved, it is run again with the corrected reflectivity to consider the attenuation by water drops (Lhermitte, 1990). The water content is then averaged temporally to match the RL temporal resolution of 10 min.

Figures 1c and 1d show an example of the KAZR reflectivity and KAZR-retrieved water content, respectively, for January 28, 2013 over SGP. The radar-retrieved water content profiles are considered during the intervals of opaque cloudy-sky times from 18 to 21 UTC.

When available, the cloud liquid water path (LWP) retrieved from the radar is scaled to match the LWP from the ground-based microwave radiometer (MWR; Gaustad et al., 2011). The temporal resolution of the MWR is 20 s and it is averaged to match the RL temporal resolution of 10 min. If MWR observations are unavailable, a fit between the radar-retrieved LWP and MWR LWP from all collocated observations in each month is utilized to scale the radar-retrieved LWP. We scale the radar-retrieved cloud LWC using MWR LWP for liquid clouds since we have much more confidence on the latter based on the quantified uncertainties (Gaustad et al., 2011). An example of the collocated radar-retrieved and MWR

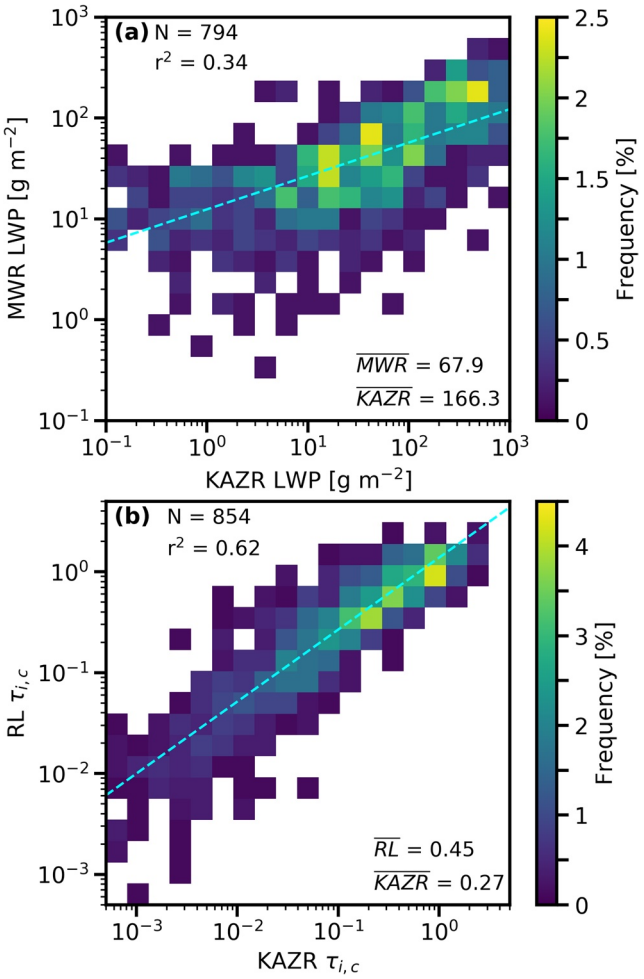

Figure 3. Frequency histogram of collocated (a) Ka-band ARM radar (KAZR) and microwave radiometer (MWR) cloud liquid water path (LWP) and (b) KAZR and Raman lidar (RL) ice cloud column optical depth for January 2013. The regression lines are shown as dashed light blue lines. The sample size (N) and coefficient of determination (r^2) are given in the top left of each plot. The mean value of KAZR ($\overline{KAZR}$), MWR ($\overline{MWR}$), and RL ($\overline{RL}$) observations are shown in the bottom right.

LWP observations for January 2013 is shown in Figure 3a where the orthogonal distance regression line is obtained by using 794 pairs of LWP observations with a coefficient of determination (r^2) of 0.34. The fitting is applied to each month to find a scaling relationship that is, then applied to the opaque cloudy-sky LWC profile when the MWR is not available.

Similar to the LWC scaling, we scale the radar-retrieved cloud IWC using RL cloud optical depth for ice clouds since again we have more confidence on the RL retrieval based on associated uncertainty (Balmes et al., 2019; Thorsen & Fu, 2015a). The radar-retrieved IWC profiles in opaque cloudy-sky conditions are scaled as follows. The scaling relationship is found by using collocated observations of radar-retrieved and RL ice cloud column optical depth when the RL is transparent. The ice cloud column optical depth is further restricted to vertical levels where both instruments detect ice clouds. The effective radius of ice particles as a function of temperature following Heymsfield et al. (2014) is used along with the radar-retrieved IWC profile to obtain its ice cloud optical depth. An example of the collocated radar-retrieved and RL ice cloud column optical depth for January 2013 is shown in Figure 3b where there are 854 collocated observations and the orthogonal distance regression line has a of 0.62. A scaling relationship is found for each month and each opaque cloudy-sky IWC profile is then scaled accordingly.

2.2. Radiative Transfer Model and Other Data

The radiative transfer model and remaining data utilized in this study, which are the same as those used in Wu et al. (2021), are briefly described below. For further details, see Sections 2 and 3 in Wu et al. (2021).

The aerosol and cloud profiles are inputted into the NASA Langley Fu-Liou radiative transfer model (Fu, 1996; Fu & Liou, 1992, 1993; Fu et al., 1998; Rose & Charlock, 2002; Rose et al., 2006). In this study, we only consider the shortwave (SW) fluxes since the longwave aerosol DRE is orders of magnitude smaller for aerosols common at SGP (e.g., Reddy et al., 2005).

In addition to the RL aerosol extinction profiles, other column-mean aerosol properties come from the AERONET Version 3 (V3) Level 2 AOD and Level 1.5 AEROSOL INVERSIONS data sets for spectral AOD, single-scattering albedo, and asymmetry factor (Giles et al., 2019). The Angstrom exponent is used for the AOD at wavelengths outside the observational spectral range. For the spectral range beyond the observed wavelengths, the single-scattering albedo and asymmetry factor are constructed from a combination of 84% urban and 16% sulfate droplets (based on the aerosol models of D'Almeida et al., 1991 and Hess et al., 1998), which best matched the AERONET spectral single-scattering albedo observations (Wu et al., 2021).

The MODerate Resolution Imaging Spectroradiometer (MODIS) MCD43C1 Version 6 Bidirectional Reflectance Distribution Function and Albedo Model Parameters data set (Roesch et al., 2004; Schaaf et al., 2002) is utilized for the surface albedos. Atmospheric state profiles are from radiosondes for temperature and water vapor, and from the European Center for Medium-Range Weather Forecasts (ECMWF) reanalysis product, ERA-Interim (Dee et al., 2011) for ozone. National Oceanic and Atmospheric Administration (NOAA) Global Monitoring Laboratory observations of trace gas concentrations of CO_2, N_2O, CH_4, and CFCs are also used.

Surface SW flux observations are from the ARM QCRAD data product (Long & Shi, 2006, 2008). The downwelling surface SW fluxes considered are the direct ($F^{\downarrow}_{direct}$), diffuse ($F^{\downarrow}_{diffuse}$), and the sum of the direct and diffuse, or the total ($F^{\downarrow}_{total}$) at the horizontal surface. The simulated downwelling surface SW fluxes are compared with observed downwelling surface SW fluxes for cloudy-sky conditions through a radiative closure experiment in the next section.

3. Radiative Closure Experiment

Simulated surface SW broadband radiative fluxes based on cloudy-sky observed inputs are compared with radiometer observations to evaluate the radiative transfer model with the observed input, which is commonly referred to as a radiative closure experiment (e.g., Comstock et al., 2013; Mace et al., 2006; Mather et al., 2007; McComiskey & Ferrare, 2016; Michalsky et al., 2006; Miller & Slingo, 2007; Shupe et al., 2015). Radiative closure experiments typically focus on clear-sky observations and only limited case studies have been done at the SGP site for cloudy-skies for SW downwelling fluxes (e.g., Lane et al., 2002; Min et al., 2003; Turner et al., 2007).

In Wu et al. (2021), we compared simulated and observed surface SW fluxes for clear-skies at SGP and found excellent agreement with a mean difference of 1 W m^{-2} in $F^{\downarrow}_{total}$. In this study, we investigate the cloudy-sky radiative closure by considering transparent cloudy-sky profiles and opaque cloudy-sky profiles separately. For the opaque cloudy-sky profiles, we consider cases with collocated RL, radar, and MWR observations. The radiative transfer model inputs (e.g., aerosol and cloud optical properties, surface albedo, atmospheric state) are detailed in Section 2.

To limit the impact of cloud horizontal inhomogeneity that cannot be observed by the zenith-view of the RL and radar for given time, we only consider cases when the observed $F^{\downarrow}_{direct}$ is greater (less) than 10 W m^{-2} for the transparent (opaque) cloudy-sky situation, and the cosine of the solar zenith angle (SZA) is greater than 0.15. Figure 4 compares the simulated and observed fluxes for the transparent cloudy-sky (Figure 4a) and opaque cloudy-sky (Figure 4b) profiles.

For the transparent cloudy-skies, the mean (relative) differences in $F^{\downarrow}_{total}$, $F^{\downarrow}_{direct}$, and $F^{\downarrow}_{diffuse}$ are 31.85 (6.0%), 37.71 (10.8%), and −5.87 (−3.3%) W m^{-2}, respectively. The correlation coefficients between simulated and observed fluxes for $F^{\downarrow}_{total}$, $F^{\downarrow}_{direct}$, and $F^{\downarrow}_{diffuse}$ are 0.76, 0.66, and 0.83, respectively. The overestimation of simulated $F^{\downarrow}_{direct}$ indicates that the cloud optical depth in the direction of the solar direct beam is generally larger than the RL-derived cloud optical depth divided by the cosine of the SZA, which might be largely caused by the cloud horizontal inhomogeneity. The exponential relationship between the optical depth and $F^{\downarrow}_{direct}$ could potentially result in the 10 min averaged observed flux to exceed the 10 min modeled flux (based on the average optical depth). However, the opposite bias is seen as there is a positive bias in the simulated $F^{\downarrow}_{direct}$, which suggest that any nonlinearity effects are compensated by another dominant factor.

For the opaque cloudy-skies, the mean differences in $F^{\downarrow}_{total}$ and $F^{\downarrow}_{diffuse}$ are −13.23 and −11.85 W m^{-2}, respectively, corresponding to relative differences of ~−7.2% and −6.5%. The correlation coefficients between modeled fluxes and observations are 0.86 for both $F^{\downarrow}_{total}$ and $F^{\downarrow}_{diffuse}$.

The sensitivity of the results to the SZA is assessed by considering stricter SZA thresholds (e.g., cos(SZA) > 0.3). For increasing cos(SZA), the transparent cloudy-sky results switch from a positive bias in $F^{\downarrow}_{total}$ and $F^{\downarrow}_{direct}$ to a negative bias while the $F^{\downarrow}_{diffuse}$ negative bias increases. For example, the relative differences in $F^{\downarrow}_{total}$, $F^{\downarrow}_{direct}$, and $F^{\downarrow}_{diffuse}$ are ~ −6.7%, −6.8%, and −6.5% when considering only profiles when cos(SZA) > 0.8. The opaque cloudy-sky radiative closure results were largely invariant of the SZA threshold and the mean difference in $F^{\downarrow}_{total}$ was ~−13 W m^{-2} and $F^{\downarrow}_{diffuse}$ was ~−12 W m^{-2} for nearly all SZA thresholds considered.

The sensitivity of the results to the observed $F^{\downarrow}_{direct}$ threshold (10 W m^{-2}) is examined by considering all transparent and opaque cloudy-sky profiles. For transparent cloudy-sky profiles, the mean differences in $F^{\downarrow}_{total}$, $F^{\downarrow}_{direct}$, and $F^{\downarrow}_{diffuse}$ are 34.36, 38.49, and −4.13 W m^{-2}, respectively, corresponding to relative differences of ~6.7%, 11.4%, and −2.3%. For the opaque cloudy-skies, the mean differences in $F^{\downarrow}_{total}$, and $F^{\downarrow}_{diffuse}$ are

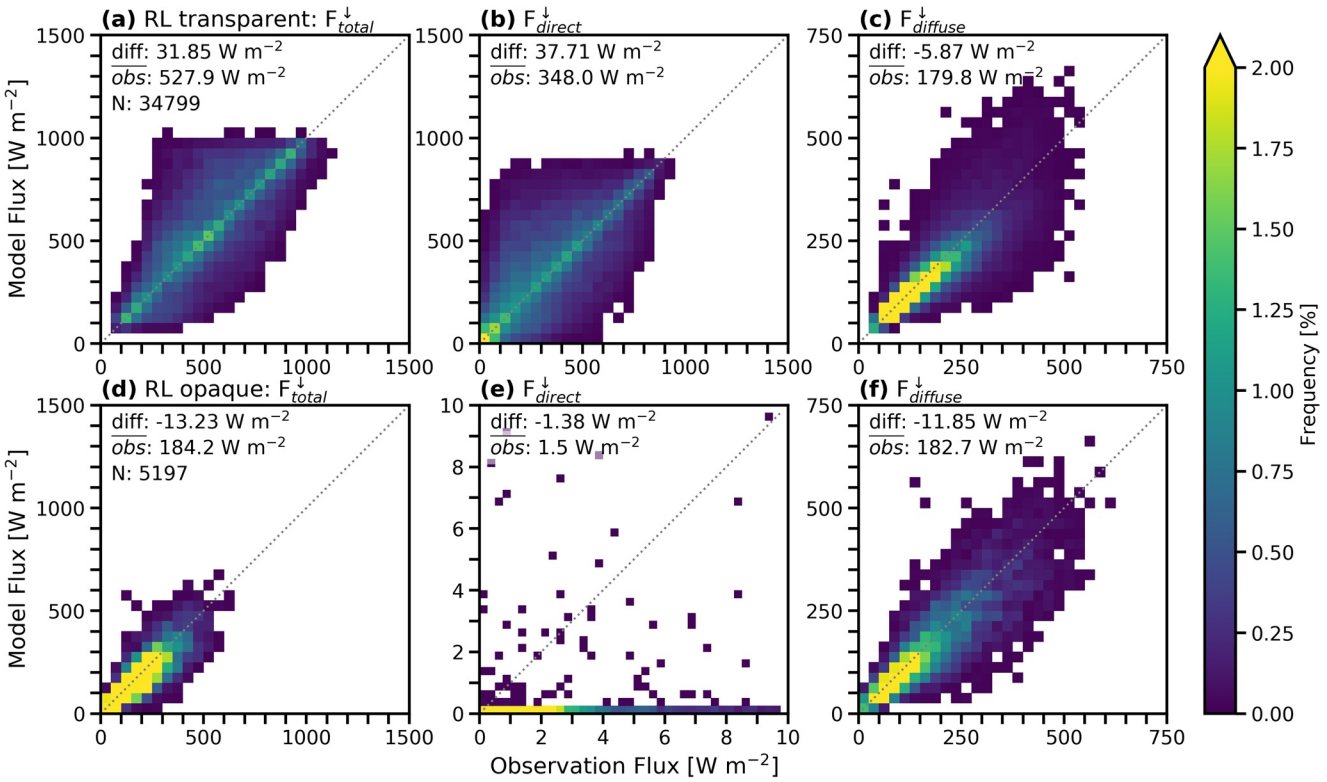

Figure 4. Downwelling surface shortwave (SW) fluxes from the model and observations. The fluxes shown include (a, d) the total downwelling surface SW fluxes, $F^{\downarrow}_{total}$, (b, e) the direct downwelling surface SW fluxes, $F^{\downarrow}_{direct}$, and (c, f) the diffuse downwelling surface SW fluxes, $F^{\downarrow}_{diffuse}$. Results are for Raman lidar (RL) transparent cloudy-sky profiles (top) and opaque cloudy-sky profiles (bottom) from August 2008 to August 2016. The 1:1 lines are shown as dashed gray lines. The mean difference (diff) between modeled and observed fluxes and the mean value of the observed fluxes ($\overline{obs}$) are given in the top left of each plot. The sample size (N) is given in the top left of each plot in the left column.

−43.50 and −9.37 W m^{-2}, respectively, corresponding to relative differences of ~−16.6% and −4.1%. While the results indicate a worse agreement in $F^{\downarrow}_{total}$ for the opaque cloudy-sky, the results are similar overall and even better in $F^{\downarrow}_{diffuse}$.

Overall, the agreement is good as the mean difference is smaller than about 10% with large correlation coefficients. While the mean differences were significantly smaller for clear-sky conditions (Wu et al., 2021), some disagreement for cloudy-sky conditions is expected since the cloud fields are horizontally heterogeneous and therefore difficult to capture with zenith-pointing instruments. In addition, the 3D effects of radiative transfer are not captured by using a 1D radiative transfer model (e.g., Fu et al., 2000).

Another reason for the disagreement could be related to errors in retrieved cloud optical depth. By decreasing the opaque cloudy-sky cloud optical depth by 10%, the mean difference between the observed and simulated fluxes becomes less than 2 W m^{-2} for $F^{\downarrow}_{total}$ and less than 1 W m^{-2} $F^{\downarrow}_{diffuse}$. For the transparent cloudy-sky situation, however, an increase or decrease in cloud optical depth only leads to a small change in the $F^{\downarrow}_{total}$ since the changes in the $F^{\downarrow}_{direct}$ and $F^{\downarrow}_{diffuse}$ are opposite in sign and largely cancel each other. For example, when the transparent cloudy-sky cloud optical depth is increased by 10%, the mean (relative) differences in $F^{\downarrow}_{total}$, $F^{\downarrow}_{direct}$, and $F^{\downarrow}_{diffuse}$ are 30.08 (5.7%), 31.79 (9.1%), and −1.71 (−0.9%) W m^{-2}, respectively. This suggests that the mean differences between observed and simulated fluxes for the transparent cloudy-sky are likely related to the cloud inhomogeneity and 3D effects. It is also worth noting that we have confidence on the transparent cloudy-sky cloud optical depth in the zenith direction based on RL observations. It will be shown later (Table 1) that the aerosol DRE is less sensitive to changes in cloud microphysical and opti-

Table 1
The Measurement Uncertainty (W m^{-2}) in Annual Mean Aerosol Direct Radiative Effect (DRE) Under All-Sky Conditions

TOA DRE uncertainty [W m^{-2}]	
AOD	±0.14 (∓6.7%)
$\overline{\omega}$	±0.47 (∓21.8%)
$\overline{g}$	±0.15 (∓6.8%)
α_s	±0.18 (∓8.2%)
$\tau(cloud, trans.)$	±0.01 (∓0.5%)
LWP	±0.02 (∓0.8%)
$\tau(ice, opaq.)$	±0.001 (∓0.06%)
r_e	±0.04 (∓1.7%)
D_{ge}	±0.01 (∓0.5%)
total	±0.54 (∓25.3%)
SFC DRE uncertainty [W m^{-2}]	
AOD	±0.45 (∓7.5%)
$\overline{\omega}$	±0.71 (∓12.0%)
$\overline{g}$	±0.15 (∓2.5%)
α_s	±0.14 (∓2.3%)
$\tau(cloud, trans.)$	±0.02 (∓0.3%)
LWP	±0.02 (∓0.4%)
$\tau(ice, opaq.)$	±0.003 (∓0.04%)
r_e	±0.05 (∓0.8%)
D_{ge}	±0.02 (∓0.3%)
total	±0.87 (∓14.5%)

Note. The uncertainty is shown for (top) the top of atmosphere (TOA) and (bottom) the surface (SFC) at the Southern Great Plains (SGP) site. The aerosol DRE uncertainty is separated into the uncertainty due to measurement uncertainty of the aerosol optical depth (AOD), column-mean single-scattering albedo ($\overline{\omega}$), column-mean asymmetry factor ($\overline{g}$), surface albedo (α_s), transparent cloud optical depth ($\tau(cloud, trans.)$), cloud liquid water path (LWP), opaque ice cloud optical depth ($\tau(ice, opaq.)$), liquid cloud particle size (r_e), ice cloud particle size (D_{ge}), and the total uncertainty considering all components. The difference relative to the annual mean aerosol DRE are given in the parentheses.

cal properties. For example, a 10% change in the transparent cloud optical depth results in a less than 1% change in the aerosol DRE (the impact of a 10% change in the opaque cloud optical depth is even smaller).

4. All-Sky Aerosol Direct Radiative Effect

The instantaneous aerosol DRE is defined as:

$$DRE = [F^{\downarrow} - F^{\uparrow}]_{aerosol} - [F^{\downarrow} - F^{\uparrow}]_{no\ aerosol,} \quad (1)$$

where $F^{\downarrow}$ is the downward flux and $F^{\uparrow}$ is the upward flux. Equation 1 is evaluated considering fluxes at the TOA for the TOA aerosol DRE and at the surface (SFC) for the SFC aerosol DRE. The aerosol DRE is calculated by running the radiative transfer model with and without aerosols for the same atmospheric profile.

The aerosol DRE is considered across three time scales in this study, including the (a) daily, (b) monthly, and (c) annual mean aerosol DREs.

The daily mean aerosol DRE, $\overline{DRE}$, is calculated as:

$$\overline{DRE} = \frac{1}{24\ hr}\int_{sunrise}^{sunset} DRE(t)dt, \tag{2}$$

where $DRE(t)$ is the instantaneous aerosol DRE at given time t. The SZA effects on the daily mean aerosol DRE are characterized by considering a time step of 30 min (Balmes & Fu, 2020; Yu et al., 2004, 2006). Note that the instantaneous aerosol DREs (e.g., Oyola et al., 2019) can be much larger than the daily mean aerosol DREs presented in this study.

4.1. Daily- and Monthly-Mean Time Series of All-Sky Aerosol DREs

The daily mean all-sky aerosol DRE is calculated by considering the instantaneous aerosol DRE at every 30 min time step. We consider the closest RL observation in time. When the closest RL observation is clear-sky or transparent cloudy-sky, the RL aerosol and cloud extinction profile is used. When the closest RL observation is opaque cloudy-sky, the closest radar cloud water content and RWC profiles are used (Section 2.1.2). The AODs used in the aerosol DRE calculations are scaled so that the (a) monthly mean AOD matches the monthly mean observed AOD (Wu et al., 2021), and that the (b) monthly mean clear-sky RL AOD matches the monthly mean AERONET AOD. The closest AERONET observations of spectral AOD, single-scattering albedo, and asymmetry factors are used if they are available within one week. If no AERONET observation is available within one week, monthly mean AERONET observations are inputted.

If the closest RL observation is beyond 1 h, we do not calculate the instantaneous aerosol DRE for that 30 min time step. In addition, if the closest radar observation is beyond 1 h of the opaque cloudy-sky observation, the instantaneous aerosol DRE is not calculated. The daily mean all-sky aerosol DRE is not estimated for days in which any 30 min time step does not have an instantaneous aerosol DRE estimate. This results in 2,030 days with a daily mean all-sky aerosol DRE estimate out of the 2,953 days from August 2008 to August 2016. Monthly mean aerosol DREs are constructed by taking the mean of all daily mean estimates in each month.

The 2,030 days with daily mean aerosol DRE estimates corresponds to 51,915 time steps of daylight when considering 30 min resolution. 91% of the time steps are within the RL profile time interval (i.e., 10 min). When they are not, the average time difference between the RL profile central time and the 30 min time step is 7.7 min. Of the time steps that are opaque cloudy-sky, 98% of radar profile times are the same time as the RL profile time. 70% of the opaque cloudy-sky time steps have MWR observations within 1 h, and 39% are within the MWR time interval. 93% of the time steps have AERONET AOD observations within 1 week and 89% of the time steps have AERONET single-scattering albedo and asymmetry factor observations within 1 week.

Figure 5 shows the daily mean all-sky aerosol DRE time series at both the TOA and the surface. The daily mean aerosol TOA DRE at SGP is typically negative with the largest in magnitude negative DRE of $-13.42\ W\ m^{-2}$. In 259 days (12.8%) of the total 2,030 days, the daily mean aerosol DRE is positive with a largest in magnitude positive DRE of $11.38\ W\ m^{-2}$. The daily mean aerosol DRE at the surface is always negative with a maximum that is nearly neutral ($-0.05\ W\ m^{-2}$) to a minimum of $-34.87\ W\ m^{-2}$. Figure 5 also shows the monthly mean aerosol DRE time series. The monthly mean aerosol DRE varied from 2.24 to $-5.83\ W\ m^{-2}$ at the TOA and from -1.27 to $-13.75\ W\ m^{-2}$ at the surface. Two months have a positive monthly mean aerosol DRE at the TOA (September 2010 and October 2013), while all other 89 monthly mean aerosol DREs are negative. In contrast to the clear-sky aerosol DRE, the all-sky aerosol DRE is typically less negative due to the increased albedo by the clouds, which tends to weaken the aerosol DRE. Consider the clear-sky aerosol DRE in the same 2,030 days at SGP for a comparison: the TOA daily mean aerosol DRE is positive only for 27 days (1.3%) with a maximum value of $2.04\ W\ m^{-2}$. In addition, the TOA monthly mean aerosol DRE ranges from -0.60 to $-7.19\ W\ m^{-2}$. Similar to the clear-sky aerosol DRE, the all-sky aerosol DRE is generally stronger (i.e., more negative) during the summer and weaker (i.e., less negative) during the winter. This is

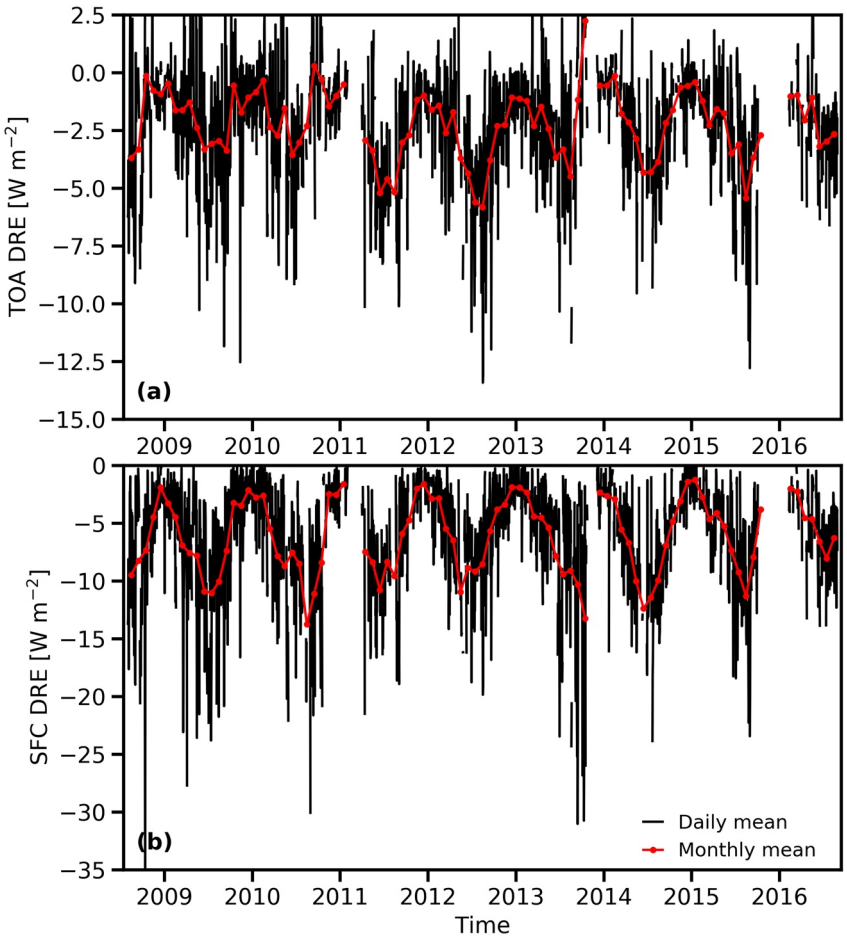

Figure 5. The daily mean (black) and monthly mean (red) all-sky aerosol direct radiative effect (DRE) time series at the Southern Great Plains (SGP) site from August 2008 to August 2016. Results are shown for (a) the top of the atmosphere (TOA) and (b) surface (SFC).

related to the seasonal cycle of AOD and daytime fraction, which are both larger in the summertime. The all-sky aerosol DRE seasonal cycle is investigated in more detail in the next section.

4.2. Seasonal Cycle and Annual Mean All-Sky Aerosol DRE

The seasonal cycle of the all-sky aerosol DRE is examined by constructing its monthly mean climatology, which is the mean of all monthly mean estimates for each month. The annual mean climatology of the aerosol DRE is then the mean of the monthly mean climatology. Since the daily mean aerosol DRE is not estimated for all 2,953 days of the 8 yr study period, its impact on the annual mean aerosol DRE is assessed. The clear-sky annual mean aerosol DRE in Wu et al. (2021) is calculated using all 2,953 days, which differed from that by considering the 2,030 days by only 0.02 W m^{-2} at both the TOA and surface. This provides confidence that the all-sky aerosol DRE result presented here is capturing the annual mean aerosol DRE despite missing days due to unavailable observations.

Figure 6 shows the seasonal cycle of the all-sky aerosol DRE, which largely follows the seasonal cycle of the clear-sky aerosol DRE in Wu et al. (2021) (also shown in Figure 6 for a comparison) with secondary effects from clouds. The strongest aerosol DREs of −3.90 W m^{-2} at the TOA and −9.41 W m^{-2} at the surface are during the summer (June–August) when the AOD is largest. The weakest aerosol DREs correspond to October–February with −1.01 W m^{-2} at the TOA and −3.31 W m^{-2} at the surface.

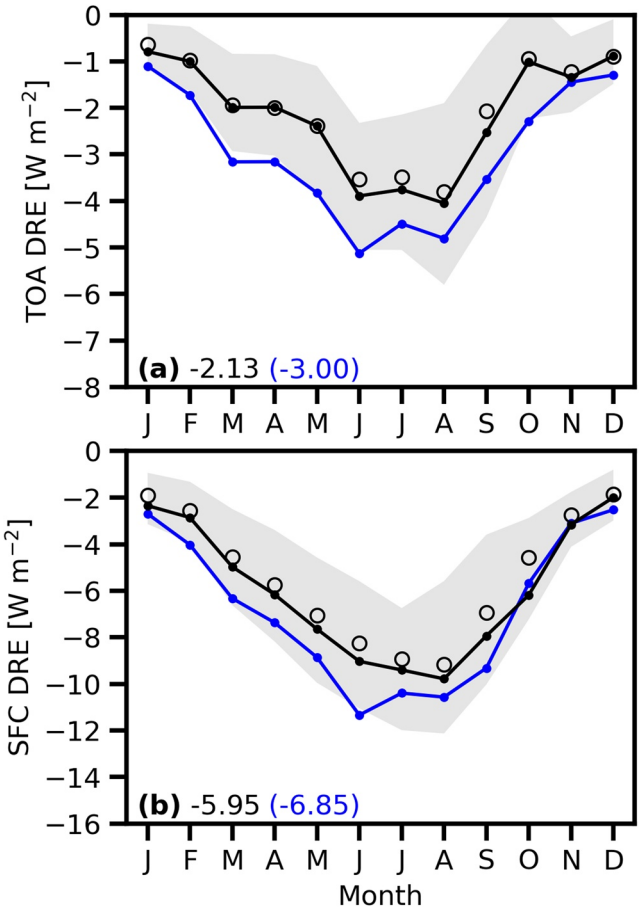

Figure 6. Seasonal cycle of aerosol direct radiative effect (DRE) at the Southern Great Plains (SGP) site from August 2008 to August 2016. Results are shown for (a) the top of the atmosphere (TOA) and (b) the surface (SFC). The aerosol DRE mean (black dots), median (black open circles), and 25th–75th percentile of daily means (shading) are shown. The annual mean climatology values are given in the bottom left. The clear-sky monthly mean climatology is shown in blue along with the annual mean climatology value given in the parentheses for a comparison.

The annual mean all-sky aerosol DRE climatology is −2.13 and −5.95 W m^{-2} at the TOA and surface, respectively. In comparison to the annual mean clear-sky aerosol DRE, the all-sky aerosol DRE is weaker by 0.86 (0.90) W m^{-2} or by 28.8% (13.1%) at the TOA (surface). This is what we expect since the clouds overall weaken the aerosol DRE. The relative difference is comparable to other studies that provide both a clear-sky and all-sky aerosol DRE estimate (e.g., Matus et al., 2015). The annual mean aerosol DRE shows interannual variability (Figure 5), which for the all-sky (clear-sky) conditions ranges from −1.60 W m^{-2} in 2010 (−2.52 W m^{-2} in 2010) to −3.02 W m^{-2} in 2012 (−3.79 W m^{-2} in 2012) at the TOA and from −5.24 W m^{-2} in 2015 (−6.24 W m^{-2} in 2011) to −6.82 W m^{-2} in 2010 (−7.55 W m^{-2} in 2009) at the surface.

The all-sky aerosol DRE can be separated into the contribution from clear-sky, transparent cloudy-sky, and opaque cloudy-sky. For the annual mean climatology at the TOA (surface), the contributions are −1.15 (−2.89) W m^{-2} from clear-skies, −1.04 (−2.45) W m^{-2} from transparent cloudy-skies, and 0.06 (−0.61) W m^{-2} for opaque cloudy-skies. About 50% contribution each from clear-sky and transparent cloudy-sky varies little from month to month (not shown). The transparent cloudy-sky contribution that is, nearly the same as that from clear-sky is a result of cancellation effects in the transparent cloudy-sky. The transparent cloudy-sky AOD is larger than the clear-sky AOD (Balmes et al., 2021), which strengthens the aerosol DRE. However, the weakening in aerosol DRE due to cloud reflection overall compensates the strengthening due to larger AOD. The opaque cloudy-sky contribution is very small and the monthly mean climatology contribution ranges from −0.11 in July to 0.26 W m^{-2} in May, with most months less than 0.10 W m^{-2} in magnitude.

The all-sky aerosol DRE estimates in this study provide an estimate with all input quantities from observations for a point-location. This can provide a benchmark to compare with satellite and modeling estimates. We compare our all-sky estimates to those from Matus et al. (2019), which estimate the aerosol DRE globally from A-train satellite observations of clouds and aerosols on a 2.5 by 2.5° latitude-longitude grid. For the grid point covering SGP (35–37.5°N, 95–97.5°W), their all-sky aerosol TOA DRE estimate is −1.86 W m^{-2} annually. Seasonally, their all-sky aerosol TOA DRE estimate is −0.63 W m^{-2} for December–February, −2.13 W m^{-2} for March–May, −1.48 W m^{-2} for June–August, and −2.85 W m^{-2} for September–November. For a comparison, the TOA estimates presented in this study (Figure 6) are −2.13 W m^{-2} annually, −0.89 W m^{-2} for December–February, −2.12 W m^{-2} for March–May, −3.90 W m^{-2} for June–August, and −1.63 W m^{-2} for September–November. The all-sky aerosol DRE based on satellite observations over the SGP site is 38% of that from the present study in the summer but is 1.75 times of that from the present study in the fall. The latter is a surprise since CALIPSO does not detect all radiatively significant aerosols and underestimated aerosol DREs were expected (e.g., Thorsen et al., 2017; Thorsen & Fu, 2015b). Further research efforts are required to understand such discrepancy between the satellite- and ground-based estimates of the aerosol DREs.

To further interpret the differences between the clear-sky and all-sky aerosol DREs due to clouds, we examine the SW cloud radiative effect (CRE). The daily mean and seasonal cycle CRE are calculated in the same way as the aerosol DRE, except the difference in fluxes is found by running the radiative transfer model with and without clouds. The seasonal cycle of the all-sky SW CRE is shown in Figure 7. The strongest all-sky SW CRE of −60.54 (−64.69) W m^{-2} occurs in May at the TOA (surface). The stronger CRE in the springtime (March–May) corresponds to a stronger relative weakening of the all-sky aerosol TOA DRE compared to clear-sky aerosol TOA DRE (~37%). The weakest all-sky SW CRE of −16.87 (−17.54) W m^{-2} occurs in

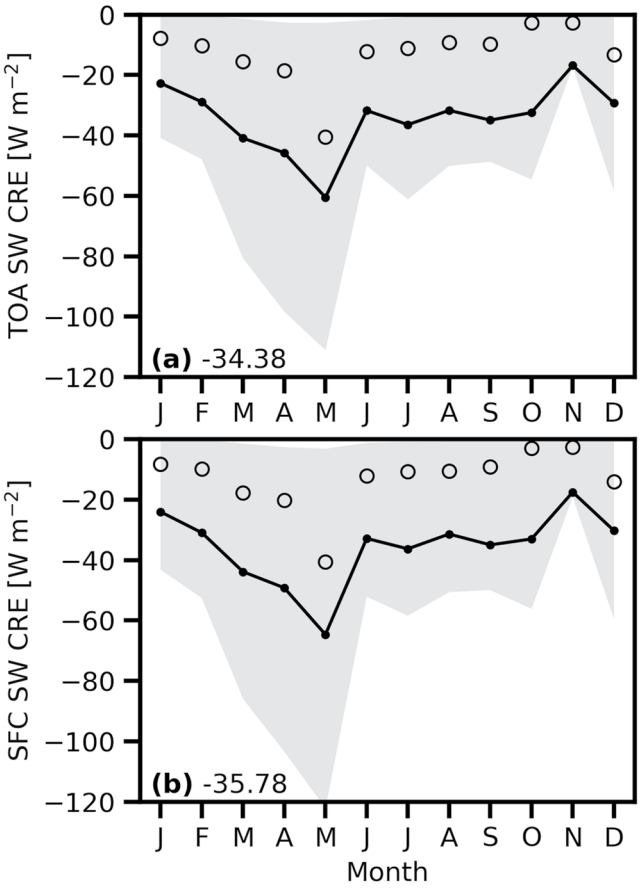

Figure 7. Seasonal cycle of the shortwave (SW) cloud radiative effect (CRE) at the Southern Great Plains (SGP) site from August 2008 to August 2016. Results are shown for the (a) top of the atmosphere (TOA) and (b) surface (SFC). The SW CRE mean (dots), median (open circles), and 25th–75th percentile (shading) are shown. The annual mean climatology values are given in the bottom left.

November at the TOA (surface), which corresponds to a small relative weakening of the all-sky aerosol TOA DRE of ~8%.

Other studies have quantified the CRE at SGP and results are comparable to those presented here. For example, Mace and Benson (2008) showed the CRE is more negative in the spring and less negative in the summer and fall and monthly mean climatology values range between ~−20 to −60 W m^{-2} at the TOA and the surface. Dong et al. (2006) also showed a similar surface all-sky CRE.

Figure 8 shows the monthly climatology of all-sky aerosol radiative heating profiles (a) and its difference from that under clear-sky conditions (b). The aerosol heating profile is calculated analogously to the aerosol DRE, but instead considering the difference in the radiative heating rate profile with and without aerosols. The all-sky heating profile is similar to the clear-sky heating profile in Wu et al. (2021), which is predominantly near the surface and extends higher into the atmosphere from April to October. The all-sky heating profile is smaller than the clear-sky heating rates by ~0.07 K/day near the surface and is also slighter smaller between ~0.3 and 1.5 km (Figure 8b; with the exception in October). The reduced radiative heating rate in the lower atmosphere and near the surface is due to clouds reflecting downwelling SW radiation, which overall reduces the downwelling solar radiation there. The heating is slightly stronger than the clear-sky heating rates around 2–3 km due to aerosol heating above clouds that reflect downwelling SW radiation and thus increase the absorption of the SW radiation by aerosols above. In October, the all-sky radiative heating is larger than the clear-sky heating including the near-surface and lower atmosphere where the impact of the larger aerosol extinction in cloudy-sky might outweigh the cloud albedo effects.

4.2.1. Sensitivity of Annual Mean All-Sky Aerosol DRE to the Methods Used

The sensitivity of annual mean all-sky aerosol DRE to the methods used is examined. Considering RL observations within 10 min instead of 1 h of each time step results in a difference of −0.04 W m^{-2} in the annual mean DRE at both the TOA and surface. The small aerosol DRE difference is largely caused by the reduction of days with aerosol DRE estimates, which becomes 1,798 days.

When the radar profile must be within 10 min instead of 1 h, the annual mean aerosol DRE differed by −0.03 W m^{-2} at both the TOA and surface and the number of days with aerosol DRE estimates is reduced to 1,956 days. MWR observations restricted to within 10 min results in an annual mean aerosol DRE difference less than 0.5%. The sensitivity of the aerosol DRE to AERONET observations within 1 week is assessed by considering observations within 1 day and the difference in aerosol DRE is found to be within 2%. Overall, the aerosol DRE annual mean estimate is largely insensitive to using observations within 1 h (or 1 week for AERONET) since the vast majority of observations are at the same time of the 30 min time steps considered or closer than the threshold considered.

The sensitivity of the aerosol DRE to the radar-retrieved water content profiles for the opaque cloudy-sky profiles are tested by using different retrievals. The radar-retrieved water content is instead retrieved following Frisch et al. (1995) for LWC, Liu and Illingworth (2000) for IWC, and Comstock et al. (2004) for RWC. In all cases, the aerosol DRE differed by less than 0.01 W m^{-2} at both the TOA and surface. This small difference is because the LWP and IWP are constrained by MWR and RL observations, respectively. The sensitivity of the aerosol DRE to the LWP scaling relationship (Figure 3a) (that is used to scale the radar-retrieved LWP when MWR observations are not available) is tested by using the scaling relationships for all LWC profile (i.e., no collocated MWR observations are used). The annual mean aerosol DRE

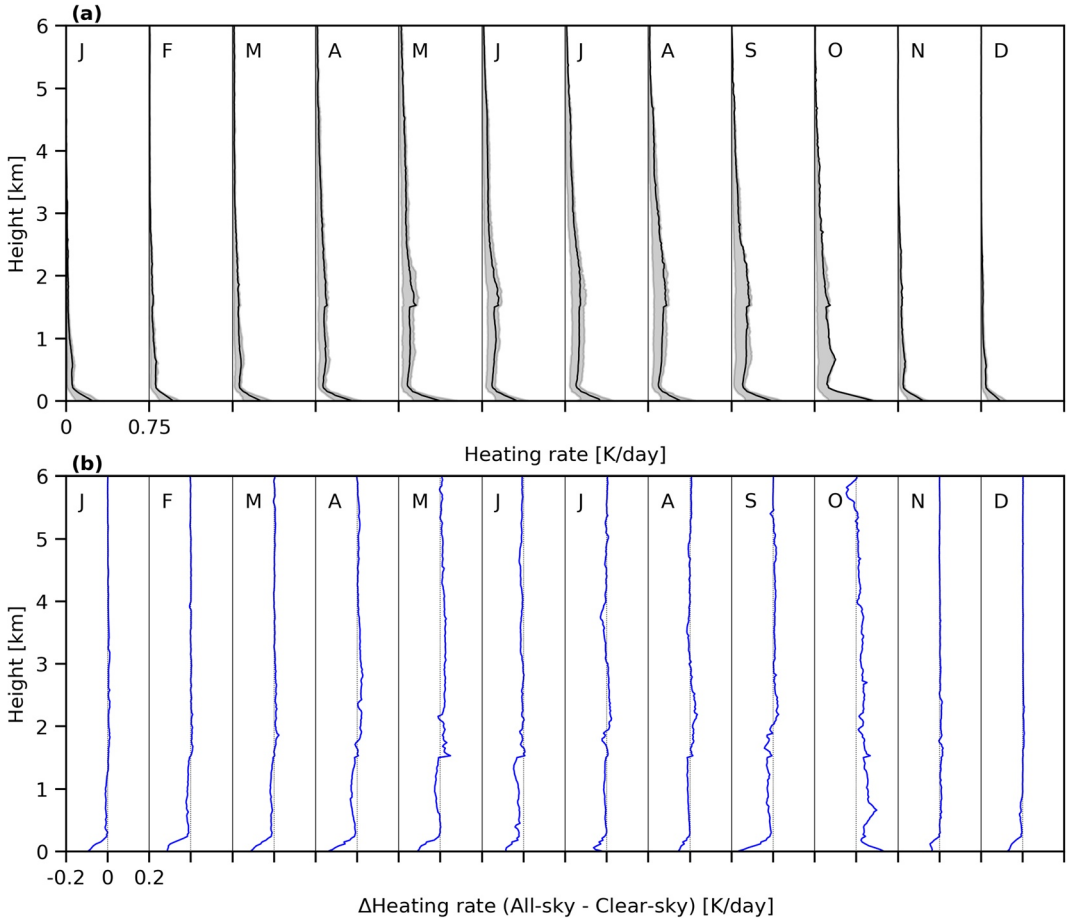

Figure 8. (a) The all-sky aerosol radiative heating rate profile monthly climatology at the Southern Great Plains (SGP) site from August 2008 to August 2016 with the 25th–75th percentile (shading). (b) The difference between the all-sky and clear-sky monthly climatology heating rate profiles (blue line).

differed by 0.01 W m^{-2} or less, providing confidence that the scaling relationships used are representative in regards to estimating the aerosol DRE. The sensitivity of the LWP scaling relationship (Figure 3a) is further tested by restricting profiles to those where the MWR LWP is greater than 10 g m^{-2}. The annual mean aerosol DRE differed only by 0.2% (0.1%) at the TOA (surface), showing that the aerosol DRE is insensitive to the opaque cloudy-sky LWP.

The sensitivity of the aerosol DRE to the opaque cloudy-sky aerosol profile is also tested. The monthly mean aerosol extinction profile was used for the heights above where the RL fully attenuated instead of the weekly mean, which resulted in a difference of 0.01 W m^{-2} at both the TOA and surface. Additionally, the weekly mean aerosol extinction profile was also used for heights where clouds or precipitation were detected by the radar instead of considering the aerosol extinction to be zero. The annual mean aerosol DRE differed by 0.09 (−0.32) W m^{-2} at the TOA (surface), which is −4.3% (5.4%) of the annual mean.

5. Aerosol DRE Uncertainty Estimates Associated With Measurements

In Wu et al. (2021), we estimated the measurement uncertainty and methodology uncertainty in the estimated clear-sky aerosol DRE. This section focuses on the measurement uncertainty in the estimated all-sky aerosol DRE. See Wu et al. (2021) and Section 4.2.1 for the methodology uncertainty. In contrast to the clear-sky aerosol DRE uncertainty estimates, this study will instead apply the measurement uncertainties to each model run instead of running one profile for each month with monthly mean climatological aero-

sol optical properties. For AOD, single-scattering albedo, asymmetry factor, and surface albedo, the same uncertainty considered for the clear-sky aerosol DRE will be applied to quantify the all-sky aerosol DRE measurement uncertainty (see Section 6.1.1 in Wu et al., 2021 for specifics). Note that the uncertainty in the single-scattering albedo is provided for each available AERONET retrieval as a 1-sigma estimate for each observational wavelength (i.e., 440, 675, 870, and 1,020 nm). We derive the mean single-scattering albedo uncertainty estimate for each wavelength by averaging the individual single-scattering albedo uncertainty weighted by the optical depth. We then apply this single-scattering albedo uncertainty interpolated to model wavelengths to estimate the impact on the aerosol DRE. In addition to aerosol optical properties, measurement uncertainties associated with clouds due to optical depth, LWP, and particle size will also be quantified.

The annual-mean uncertainty estimates are presented in Table 1. In general, the relative (absolute) uncertainties in all-sky aerosol DRE due to aerosol optical properties are similar to those for clear-sky (see Table 1 in Wu et al., 2021). For example, the annual mean aerosol DRE uncertainty due to AOD is about ± 7%–8% at the TOA and the surface, compared to ±8% for clear-sky. The exception is the uncertainty in the TOA aerosol DRE due to the aerosol single-scattering albedo, which is 22% in all-sky but 15% in clear-sky. The single-scattering albedo measurement uncertainty is again the largest contributor to the measurement uncertainty, which is consistent with McComiskey et al. (2008) and Thorsen et al. (2020, 2021). Compared to clear-sky, the asymmetry factor and surface albedo measurement uncertainty are slightly higher at the TOA (±7%–8%) but slightly lower at the surface (±2%–3%).

The aerosol DRE uncertainties due to cloud properties measurements are also quantified in Table 1. The cloud measurement uncertainties are separated into those from the transparent cloudy-sky optical depth, the opaque cloudy-sky LWP, and the opaque cloudy-sky ice cloud optical depth. For the transparent cloudy-sky optical depth, the mean relative cloud column optical depth uncertainty is based on the RL-FEX reported extinction systematic uncertainty, which is found to be ~ ±10%, resulting in an uncertainty in the annual mean aerosol DRE of ~0.01 W m^{-2} at the TOA and ~0.02 W m^{-2} at the surface.

For the opaque cloudy-sky LWP, the mean relative uncertainty is based on the MWR-reported LWP uncertainty of ±10%, resulting in the all-sky aerosol DRE uncertainty of less than 1% at both the TOA and the surface. While the measurement uncertainty in LWP of ±10% is the uncertainty considered in this study, when considering an uncertainty of ±20% in LWP, the aerosol DRE uncertainty is 2% at the TOA and 1% at the surface. This further demonstrates that large errors in opaque cloudy-sky LWP does not impact the aerosol DRE. The opaque cloudy-sky ice cloud optical depth uncertainty is considered to be similar to that for the transparent ice cloudy-sky condition since the opaque cloudy-sky IWC profile is scaled using a relationship based on the transparent RL ice cloud optical depth. The relative uncertainty is ±5%, resulting in an uncertainty in the aerosol DRE of less than 0.1% at the TOA and surface.

The liquid cloud particle size uncertainty considered is ±1.91 microns for transparent cloudy-skies (Thorsen & Fu, 2015a) and ±10% for opaque cloudy-skies (Zhao et al., 2012). The resulting aerosol DRE uncertainty is 2% at the TOA and 1% at the surface. The ice cloud particle size uncertainty is also considered to be ±10%, which results in an all-sky aerosol DRE uncertainty of less than 1% at both the TOA and the surface. The small uncertainty in the opaque cloudy-sky terms is expected since the opaque cloudy-sky contribution is overall very small (Section 4.2).

The total aerosol DRE uncertainty estimate associated with measurement uncertainties is quantified in the same manner as Equation 4 of Wu et al. (2021) by adding the uncertainties in quadrature, but with additional terms for the uncertainties associated with the cloud properties. The monthly aerosol DRE with the total monthly measurement uncertainty is shown in Figure 9 The monthly relative uncertainty ranges between 20% and 40%. Overall, the all-sky aerosol DRE measurement uncertainties are similar to those estimated for clear-sky despite the additional cloud optical properties uncertainties. All aerosol DRE uncertainties due to cloud optical properties uncertainty are 2% or less, which are all less than the smallest clear-sky measurement uncertainty term (3%). In summary, we have annual mean aerosol DREs of −2.13±0.54 (∓25.3%) at the TOA and −5.95±0.87 (∓14.5%) at the surface under all-sky conditions, compared to −3.00±0.58 (∓19.4%) at TOA and −6.85±1.00 (∓14.6%), respectively, under clear-sky conditions.

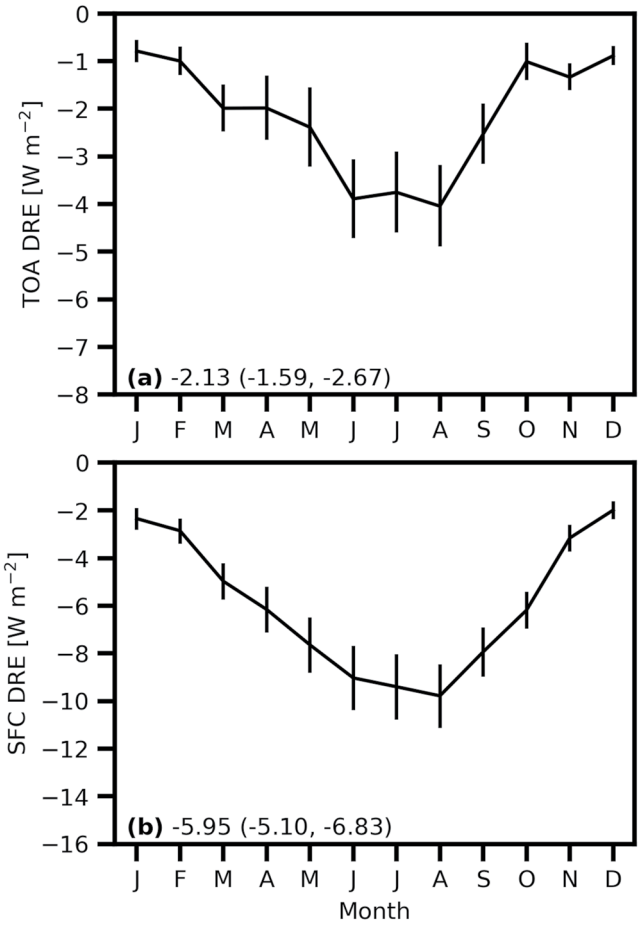

Figure 9. The all-sky aerosol direct radiative effect (DRE) seasonal cycle and the uncertainty estimate (vertical line) due to aerosol optical properties, surface albedo, and cloud properties measurements at the Southern Great Plains (SGP). Results are shown for the (a) top of the atmosphere (TOA) and the (b) surface (SFC). The monthly mean aerosol DRE is the same as those in Figure 6. The annual mean values are given in the bottom left with the range due to measurement uncertainty in the parentheses.

6. Conclusion

The all-sky aerosol DREs were estimated at the ARM SGP site using ground-based observations along with the NASA Langley Fu-Liou radiative transfer model for the first time. Previously, we quantified the clear-sky aerosol DRE by considering aerosol optical properties from the Raman lidar and AERONET, atmospheric state from radiosondes, and surface shortwave spectral albedo from radiometers. In addition to those observations, cloud extinction vertical profiles from the Raman lidar, cloud water content profiles from the MMCR and KAZR, and cloud LWP from the MWR are also considered in the all-sky aerosol DRE estimates. Simulated shortwave (SW) downwelling surface total ($F^{\downarrow}_{total}$), direct ($F^{\downarrow}_{direct}$), and diffuse ($F^{\downarrow}_{diffuse}$) fluxes were compared with observations through a radiative closure experiment for cloudy-sky conditions.

For transparent cloudy-sky profiles, the mean differences between simulated and observed SW downwelling surface fluxes were 31.85 W m^{-2}(6.0%) for $F^{\downarrow}_{total}$, 37.71 W m^{-2} (10.8%) for $F^{\downarrow}_{direct}$, and −5.87 W m^{-2} (−3.3%) for $F^{\downarrow}_{diffuse}$, which are largely related to the cloud inhomogeneity and 3D effects. The correlation coefficients between the simulated and observed fluxes were 0.76 for $F^{\downarrow}_{total}$, 0.66 for $F^{\downarrow}_{direct}$, and 0.83 for $F^{\downarrow}_{diffuse}$. For opaque cloudy-sky profiles, the mean differences between simulated and observed SW downwelling surface fluxes were −13.23 W m^{-2} (−7.2%) for $F^{\downarrow}_{total}$ and −11.85 W m^{-2} (−6.5%) for $F^{\downarrow}_{diffuse}$. The correlation coefficients between the simulated and observed fluxes were 0.86 for $F^{\downarrow}_{total}$ and $F^{\downarrow}_{diffuse}$. These differences become about 1–2 W m^{-2} by decreasing the opaque cloud optical depth by 10%.

The all-sky aerosol DRE is quantified for the daily mean, monthly mean, and annual mean. In terms of the daily mean, the aerosol DRE ranged from 11.38 to −13.42 W m^{-2} at the TOA and from −0.05 to −34.87 W m^{-2} at the surface. In terms of the monthly mean, the aerosol DRE ranged from 2.24 to −5.83 W m^{-2} at the TOA and −1.27 to −13.75 W m^{-2} at the surface. The annual mean aerosol DRE was −2.13 W m^{-2} at the TOA and −5.95 W m^{-2} at the surface, which were −3.00 W m^{-2} and −6.85 W m^{-2}, respectively, under clear-sky conditions for a comparison. Similar to the clear-sky aerosol DRE estimates in Wu et al. (2021), the seasonal cycle of the all-sky aerosol DRE largely follows the AOD seasonal cycle. Additionally, the solar insolation seasonal cycle amplifies the all-sky aerosol DRE seasonal cycle. The all-sky aerosol DRE is weaker than the clear-sky aerosol DRE by 28.8% (13.1%) at the TOA (surface) as the addition of the clouds increases the albedo.

The strongest aerosol DREs of −3.90 W m^{-2} at the TOA and −9.41 W m^{-2} at the surface are during the summer (June–August). The weakest aerosol DREs of −1.01 W m^{-2} at the TOA and −3.31 W m^{-2} at the surface are in the fall and winter (October–February). The strongest aerosol DREs correspond to the largest observed AODs while the weakest aerosol DREs correspond to smaller observed AOD and single-scattering albedo.

The all-sky aerosol DRE uncertainty estimates are quantified (Table 1). The measurement uncertainties in aerosol optical properties, surface albedo, and cloud properties result in the annual mean aerosol DREs of −2.13±0.54 (∓25.3%) at the TOA and −5.95±0.87 (∓14.5%) at the surface under all-sky conditions, compared to −3.00±0.58 (∓19.4%) at the TOA and −6.85±1.00 (∓14.6%) at the surface, respectively, under clear-sky conditions. The all-sky aerosol DRE relative uncertainty due to individual components is comparable to that for the clear-sky aerosol DRE except for the aerosol single-scattering albedo: the uncertainty in the TOA aerosol DRE due to aerosol single-scattering albedo in all-sky (22%) is larger than that in clear-sky (15%).

The regional all-sky aerosol DRE is quantified from radiative transfer modeling with high-quality ground-based aerosol and cloud observations. The all-sky aerosol DRE for one location with a suite of observations can be helpful to evaluate the estimated aerosol DRE from satellite and modeling efforts, which can further knowledge of aerosols in the climate system and constrain the aerosol direct radiative forcing, or the radiative perturbation due to anthropogenic aerosol alone.

Data Availability Statement

Data can be downloaded from the AERONET website (aeronet.gsfc.nasa.gov/new_web/data.html), USGS website (lpdaac.usgs.gov/products/mcd43c1v006/), NOAA website (www.esrl.noaa.gov/gmd/aggi/aggi.html), and ECMWF website (www.ecmwf.int/en/forecasts/datasets/reanalysis-datasets/era-interim). Data can be downloaded from the ARM data archive for the Raman lidar (adc.arm.gov/discovery/#/results/s:rlproffex1thor), radar (adc.arm.gov/discovery/#/results/s:sgparsclkazr1kolliasC1), microwave radiometer (adc.arm.gov/discovery/#/results/s:sgpmwrret1liljclouC1), and surface flux (adc.arm.gov/discovery/#/results/s:sgpqcrad1longC1).

Acknowledgments
The authors thank T. J. Thorsen for useful discussions. The authors also thank R. Marchand and R. Wood for valuable comments and suggestions. This study is supported by the U.S. Department of Energy Office of Science (BER) under Grant DE-SC0020135.

References

Ackerman, T. P., & Stokes, G. M. (2003). The atmospheric radiation measurement program. *Physics Today*, *56*(1), 38–44. https://doi.org/10.1063/1.1554135

Balmes, K. A., & Fu, Q. (2018). An investigation of optically very thin ice clouds from ground-based ARM Raman lidars. *Atmosphere*, *9*(11), 445. https://doi.org/10.3390/atmos9110445

Balmes, K. A., & Fu, Q. (2020). The diurnally averaged aerosol direct radiative effect and the use of the daytime-mean and insolation-weighted-mean solar zenith angles. *Journal of Quantitative Spectroscopy and Radiative Transfer*, *257*, 107363. https://doi.org/10.1016/j.jqsrt.2020.107363

Balmes, K. A., Fu, Q., & Thorsen, T. J. (2019). Differences in ice cloud optical depth from CALIPSO and ground-based Raman lidar at the ARM SGP and TWP sites. *Journal of Geophysical Research: Atmospheres*, *124*(3), 1755–1778. https://doi.org/10.1029/2018JD028321

Balmes, K. A., Fu, Q., & Thorsen, T. J. (2021). The diurnal variation of the aerosol optical depth at the ARM SGP site (submitted). *Earth and Space Science*.

Bansal, O., Singh, A., & Singh, D. (2019). Aerosol characteristics over the Northwestern Indo-Gangetic plain: Clear-sky radiative forcing of composite and black carbon aerosol. *Aerosol and Air Quality Research*, *19*, 5–14. https://doi.org/10.4209/aaqr.2017.09.0339

Boucher, O., Randall, D., Artaxo, P., Bretherton, C., Feingold, G., Forster, P., et al. (2013). *Clouds and aerosols*. In T. F. Stocker et al. (Ed.). Cambridge, UK. Retrieved from https://www.ipcc.ch/site/assets/uploads/2018/02/WG1AR5_Chapter07_FINAL-1.pdf

Che, H., Xia, X., Zhao, H., Dubovik, O., Holben, B. N., Goloub, P., et al. (2019). Spatial distribution of aerosol microphysical and optical properties and direct radiative effect from the China aerosol remote sensing network. *Atmospheric Chemistry and Physics*, *19*(18), 11843–11864. https://doi.org/10.5194/acp-19-11843-2019

Clothiaux, E. E., Miller, M. A., Turner, D. D., Mace, G. G., Marchand, R. T., Widener, K. B., et al. (2001). *The ARM millimeter wave cloud radars (MMCRs) and the active remote sensing of clouds (ARSCL) value added product (VAP) (Tech. Rep.)*. Washington, DC: U.S. Dep. of Energy. Retrieved from https://www.arm.gov/publications/tech_reports/arm-vap-002-1.pdf

Comstock, J. M., Protat, A., McFarlane, S. A., Delanoë, J., & Deng, M. (2013). Assessment of uncertainty in cloud radiative effects and heating rates through retrieval algorithm differences: Analysis using 3 yr of ARM data at Darwin, Australia. *Journal of Geophysical Research: Atmospheres*, *118*(10), 4549–4571. https://doi.org/10.1002/jgrd.50404

Comstock, K. K., Wood, R., Yuter, S. E., & Bretherton, C. S. (2004). Reflectivity and rain rate in and below drizzling stratocumulus. *Quarterly Journal of the Royal Meteorological Society*, *130*(603), 2891–2918. https://doi.org/10.1256/qj.03.187

Creekmore, T. N., Joseph, E., Long, C. N., & Li, S. (2014). Quantifying aerosol direct effects from broadband irradiance and spectral aerosol optical depth observations. *Journal of Geophysical Research: Atmospheres*, *119*(9), 5464–5474. https://doi.org/10.1002/2013JD021217

D'Almeida, G. A., Koepke, P., & Shettle, E. P. (1991). *Atmospheric aerosols: Global climatology and radiative characteristics*. Hampton, Virginia: A. Deepak

Dee, D. P., Uppala, S. M., Simmons, A. J., Berrisford, P., Poli, P., Kobayashi, S., et al. (2011). The ERA-interim reanalysis: Configuration and performance of the data assimilation system. *Quarterly Journal of the Royal Meteorological Society*, *137*(656), 553–597. https://doi.org/10.1002/qj.828

Delene, D. J., & Ogren, J. A. (2002). Variability of aerosol optical properties at four North American surface monitoring sites. *Journal of the Atmospheric Sciences*, *59*(6), 1135–1150. https://doi.org/10.1175/1520-0469(2002)059<1135:VOAOPA>2.0.CO;2

Di Biagio, C., di Sarra, A., & Meloni, D. (2010). Large atmospheric shortwave radiative forcing by Mediterranean aerosols derived from simultaneous ground-based and spaceborne observations and dependence on the aerosol type and single scattering albedo. *Journal of Geophysical Research*, *115*(D10). D10209. https://doi.org/10.1029/2009JD012697

Di Biagio, C., di Sarra, A., Meloni, D., Monteleone, F., Piacentino, S., & Sferlazzo, D. (2009). Measurements of Mediterranean aerosol radiative forcing and influence of the single scattering albedo. *Journal of Geophysical Research*, *114*(D6). D06211. https://doi.org/10.1029/2008JD011037

Dong, X., Xi, B., & Minnis, P. (2006). A climatology of midlatitude continental clouds from the ARM SGP Central Facility. Part II: Cloud fraction and surface radiative forcing. *Journal of Climate*, *19*(9), 1765–1783. https://doi.org/10.1175/jcli3710.1

Dunn, M., Johnson, K., & Jensen, M. (2011). *The microbase value-added product: A baseline retrieval of cloud microphysical properties (Tech. Rep.)*. Washington, DC: U.S. Dep. of Energy.

Ferrare, R., Turner, D., Clayton, M., Schmid, B., Redemann, J., Covert, D., et al. (2006). Evaluation of daytime measurements of aerosols and water vapor made by an operational Raman lidar over the Southern Great Plains. *Journal of Geophysical Research*, *111*, D05S08. https://doi.org/10.1029/2005jd005836

Frisch, A. S., Fairall, C. W., & Snider, J. B. (1995). Measurement of Stratus cloud and Drizzle parameters in ASTEX with a K α -band Doppler radar and a microwave radiometer. *Journal of the Atmospheric Sciences*, *52*(16), 2788–2799. https://doi.org/10.1175/1520-0469(1995)052<2788:moscad>2.0.co;2

Fu, Q. (1996). An accurate parameterization of the solar radiative properties of cirrus clouds for climate models. *Journal of Climate*, *9*(9), 2058–2082. https://doi.org/10.1175/1520-0442(1996)009<2058:AAPOTS>2.0.CO;2

Fu, Q., Cribb, M. C., Barker, H. W., Krueger, S. K., & Grossman, A. (2000). Cloud geometry effects on atmospheric solar absorption. *Journal of the Atmospheric Sciences*, *57*(8), 1156–1168. https://doi.org/10.1175/1520-0469(2000)057<1156:CGEOAS>2.0.CO;2

Fu, Q., Lesins, G., & Higgins, J. (1999). Aerosol direct radiative forcing: A five year climatology at the ARM SGP CART Site. *Ninth ARM science team meeting proceedings*. (pp. 1994–1997). San Antonio, Texas

Fu, Q., & Liou, K. N. (1992). On the correlated k-distribution method for radiative transfer in nonhomogeneous atmospheres. *Journal of the Atmospheric Sciences*, *49*(22), 2139–2156. https://doi.org/10.1175/1520-0469(1992)049<2139:OTCDMF>2.0.CO;2

Fu, Q., & Liou, K. N. (1993). Parameterization of the radiative properties of cirrus clouds. *Journal of the Atmospheric Sciences*, *50*(13), 2008–2025. https://doi.org/10.1175/1520-0469(1993)050<2008:POTRPO>2.0.CO;2

Fu, Q., Yang, P., & Sun, W. B. (1998). An accurate parameterization of the infrared radiative properties of cirrus clouds for climate models. *Journal of Climate*, *11*(9), 2223–2237. https://doi.org/10.1175/1520-0442(1998)011<2223:AAPOTI>2.0.CO;2

Fueglistaler, S., & Fu, Q. (2006). Impact of clouds on radiative heating rates in the tropical lower stratosphere. *Journal of Geophysical Research: Atmospheres*, *111*(23), 23202. https://doi.org/10.1029/2006JD007273

Gaustad, K. L., Turner, D. D., & McFarlane, S. A. (2011). *MWRRET value-added product: The retrieval of liquid water path and precipitable water vapor from microwave radiometer (MWR) data sets (Tech. Rep.)*. Washington, DC: US Dept. of Energy. Retrieved from https://www.arm.gov/publications/tech_reports/doe-sc-arm-tr-081.2.pdf

Giles, D. M., Sinyuk, A., Sorokin, M. G., Schafer, J. S., Smirnov, A., Slutsker, I., et al. (2019). Advancements in the Aerosol Robotic Network (AERONET) Version 3 database—Automated near-real-time quality control algorithm with improved cloud screening for Sun photometer aerosol optical depth (AOD) measurements. *Atmospheric Measurement Techniques*, *12*(1), 169–209. https://doi.org/10.5194/amt-12-169-2019

Goldsmith, J. E. M., Blair, F. H., Bisson, S. E., & Turner, D. D. (1998). Turn-key Raman lidar for profiling atmospheric water vapor, clouds, and aerosols. *Applied Optics*, *37*(21), 4979–4990. https://doi.org/10.1364/AO.37.004979

Henderson, D. S., L'Ecuyer, T., Stephens, G., Partain, P., & Sekiguchi, M. (2013). A multisensor perspective on the radiative impacts of clouds and aerosols. *Journal of Applied Meteorology and Climatology*, *52*(4), 853–871. https://doi.org/10.1175/jamc-d-12-025.1

Hess, M., Koepke, P., & Schult, I. (1998). Optical properties of aerosols and clouds: The software package OPAC. *Bulletin of the American Meteorological Society*, *79*(5), 831–844. https://doi.org/10.1175/1520-0477(1998)079<0831:OPOAAC>2.0.CO;2

Heymsfield, A., Winker, D., Avery, M., Vaughan, M., Diskin, G., Deng, M., et al. (2014). Relationships between ice water content and volume extinction coefficient from in situ observations for temperatures from 0°C to −86°C: Implications for spaceborne lidar retrievals. *Journal of Applied Meteorology and Climatology*, *53*(2), 479–505. https://doi.org/10.1175/jamc-d-13-087.1

Hogan, R. J., Mittermaier, M. P., & Illingworth, A. J. (2006). The retrieval of ice water content from radar reflectivity factor and temperature and its use in evaluating a mesoscale model. *Journal of Applied Meteorology and Climatology*, *45*(2), 301–317. https://doi.org/10.1175/jam2340.1

Holben, B. N., Eck, T. F., Slutsker, I., Tanré, D., Buis, J. P., Setzer, A., et al. (1998). AERONET—A federated instrument network and data archive for aerosol characterization. *Remote Sensing*, *66*(1), 1–16. https://doi.org/10.1016/S0034-4257(98)00031-5

Iziomon, M. G., & Lohmann, U. (2003). Characteristics and direct radiative effect of mid-latitude continental aerosols: The ARM case. *Atmospheric Chemistry and Physics*, *3*(6), 1903–1917. https://doi.org/10.5194/acp-3-1903-2003

Kacenelenbogen, M., Redemann, J., Vaughan, M. A., Omar, A. H., Russell, P. B., Burton, S., et al. (2014). An evaluation of CALIOP/CALIPSO's aerosol-above-cloud detection and retrieval capability over North America. *Journal of Geophysical Research: Atmospheres*, *119*(1), 230–244. https://doi.org/10.1002/2013jd020178

Lane, D. E., Goris, K., & Somerville, R. C. (2002). Radiative transfer through broken clouds: Observations and model validation. *Journal of Climate*, *15*(20), 2921–2933. https://doi.org/10.1175/1520-0442(2002)015<2921:RTTBCO>2.0.CO;2

Lhermitte, R. (1990). Attenuation and scattering of millimeter wavelength radiation by clouds and precipitation. *Journal of Atmospheric and Oceanic Technology*, *7*(3), 464–479. https://doi.org/10.1175/1520-0426(1990)007<0464:aasomw>2.0.co;2

Liao, L., & Sassen, K. (1994). Investigation of relationships between Ka-band radar reflectivity and ice and liquid water contents. *Atmospheric Research*, *34*(1–4), 231–248. https://doi.org/10.1016/0169-8095(94)90094-9

Liu, C. L., & Illingworth, A. J. (2000). Toward more accurate retrievals of ice water content from radar measurements of clouds. *Journal of Applied Meteorology*, *39*(7), 1130–1146. https://doi.org/10.1175/1520-0450(2000)039<1130:TMAROI>2.0.CO;2

Long, C. N., & Shi, Y. (2006). *The QCRad value added product: Surface radiation measurement quality control testing, including climatology configurable limits*. Washington, DC: Tech. Rep. No. DOE/SC-ARM/TR-074U.S. Dep. of Energy. https://doi.org/10.2172/1019540

Long, C. N., & Shi, Y. (2008). An automated quality assessment and control algorithm for surface radiation measurements. *The Open Atmospheric Science Journal*, *2*(1), 23–37. https://doi.org/10.2174/1874282300802010023

Mace, G. G., & Benson, S. (2008). The vertical structure of cloud occurrence and radiative forcing at the SGP ARM site as revealed by 8 yr of continuous Data. *Journal of Climate*, *21*(11), 2591–2610. https://doi.org/10.1175/2007JCLI1987.1

Mace, G. G., Benson, S., & Kato, S. (2006). Cloud radiative forcing at the atmospheric radiation measurement program climate research facility: 2. Vertical redistribution of radiant energy by clouds. *Journal of Geophysical Research*, *111*(D11), D11S91. https://doi.org/10.1029/2005jd005922

Mather, J. H., McFarlane, S. A., Miller, M. A., & Johnson, K. L. (2007). Cloud properties and associated radiative heating rates in the tropical western Pacific. *Journal of Geophysical Research*, *112*(D5), D05201. https://doi.org/10.1029/2006jd007555

Matus, A. V., L'Ecuyer, T. S., & Henderson, D. S. (2019). New estimates of aerosol direct radiative effects and forcing from A-train satellite observations. *Geophysical Research Letters*, *46*(14), 8338–8346. https://doi.org/10.1029/2019gl083656

Matus, A. V., L'Ecuyer, T. S., Kay, J. E., Hannay, C., & Lamarque, J.-F. (2015). The role of clouds in modulating global aerosol direct radiative effects in spaceborne active observations and the community Earth system model. *Journal of Climate*, *28*(8), 2986–3003. https://doi.org/10.1175/jcli-d-14-00426.1

McComiskey, A., & Ferrare, R. A. (2016). Aerosol physical and optical properties and processes in the ARM program. *Meteorological Monographs*, *57*, 21.1–21.17. https://doi.org/10.1175/amsmonographs-d-15-0028.1

McComiskey, A., Schwartz, S. E., Schmid, B., Guan, H., Lewis, E. R., Ricchiazzi, P., & Ogren, J. A. (2008). Direct aerosol forcing: Calculation from observables and sensitivities to inputs. *Journal of Geophysical Research*, *113*(D9), D09202. https://doi.org/10.1029/2007jd009170

Michalsky, J. J., Anderson, G. P., Barnard, J., Delamere, J., Gueymard, C., Kato, S., et al. (2006). Shortwave radiative closure studies for clear skies during the atmospheric radiation measurement 2003 aerosol intensive observation period. *Journal of Geophysical Research*, *111*, D14S90. https://doi.org/10.1029/2005jd006341

Miller, M. A., & Slingo, A. (2007). The ARM mobile facility and its first international deployment: Measuring radiative flux divergence in West Africa. *Bulletin of the American Meteorological Society*, *88*(8), 1229–1244. https://doi.org/10.1175/BAMS-88-8-1229

Min, Q.-L., Duan, M., & Marchand, R. (2003). Validation of surface retrieved cloud optical properties with in situ measurements at the Atmospheric Radiation Measurement Program (ARM) South Great Plains site. *Journal of Geophysical Research*, *108*(D17), 4547. https://doi.org/10.1029/2003jd003385

Mortier, A., Goloub, P., Derimian, Y., Tanré, D., Podvin, T., Blarel, L., et al. (2016). Climatology of aerosol properties and clear-sky shortwave radiative effects using Lidar and Sun photometer observations in the Dakar site. *Journal of Geophysical Research: Atmospheres*, *121*(11), 6489–6510. https://doi.org/10.1002/2015jd024588

Newsom, R. K. (2009). *Raman lidar (RL) Handbook (Tech. Rep.)*. Washington, DC: U.S. Dep. of Energy. Retrieved from https://www.arm.gov/publications/tech_reports/handbooks/rl_handbook.pdf

Oikawa, E., Nakajima, T., & Winker, D. (2018). An evaluation of the shortwave direct aerosol radiative forcing using CALIOP and MODIS observations. *Journal of Geophysical Research: Atmospheres*, *123*(2), 1211–1233. https://doi.org/10.1002/2017jd027247

Omar, A. H., Winker, D. M., Tackett, J. L., Giles, D. M., Kar, J., Liu, Z., et al. (2013). CALIOP and AERONET aerosol optical depth comparisons: One size fits none. *Journal of Geophysical Research: Atmospheres*, *118*(10), 4748–4766. https://doi.org/10.1002/jgrd.50330

Oyola, M. I., Campbell, J. R., Xian, P., Bucholtz, A., Ferrare, R. A., Burton, S. P., et al. (2019). Quantifying the direct radiative effect of absorbing aerosols for numerical weather prediction: A case study. *Atmospheric Chemistry and Physics*, *19*(1), 205–218. https://doi.org/10.5194/acp-19-205-2019

Reddy, M. S., Boucher, O., Balkanski, Y., & Schulz, M. (2005). Aerosol optical depths and direct radiative perturbations by species and source type. *Geophysical Research Letters*, *32*, L12803. https://doi.org/10.1029/2004gl021743

Redemann, J., Vaughan, M. A., Zhang, Q., Shinozuka, Y., Russell, P. B., Livingston, J. M., et al. (2012). The comparison of MODIS-Aqua (C5) and CALIOP (V2 & V3) aerosol optical depth. *Atmospheric Chemistry and Physics*, *12*(6), 3025–3043. https://doi.org/10.5194/acp-12-3025-2012

Roesch, A., Schaaf, C. B., & Gao, F. (2004). Use of moderate-resolution imaging spectroradiometer bidirectional reflectance distribution function products to enhance simulated surface albedos. *Journal of Geophysical Research*, *109*(D12), D12105. https://doi.org/10.1029/2004jd004552

Rogers, R. R., Vaughan, M. A., Hostetler, C. A., Burton, S. P., Ferrare, R. A., Young, S. A., et al. (2014). Looking through the haze: Evaluating the CALIPSO level 2 aerosol optical depth using airborne high spectral resolution lidar data. *Atmospheric Measurement Techniques*, *7*(12), 4317–4340. https://doi.org/10.5194/amt-7-4317-2014

Rose, F., Charlock, T., Fu, Q., Kato, S., Rutan, D., & Jin, Z. (2006). CERES Proto-edition 3 radiative transfer: Model tests and radiative closure over surface validation sites. In A. M. Society (Ed.), *12th conf. on atmospheric radiation, Amer. Meteor. Soc*. Madison, WI. Retrieved from https://ams.confex.com/ams/pdfpapers/112358.pdf

Rose, F. G., & Charlock, T. P. (2002). New Fu-Liou code tested with ARM Raman lidar aerosols and CERES In Pre-CALIPSO sensitivity study. In A. M. Society (Ed.), *11th conference on atmospheric radiation*. Ogden, UT. Retrieved from https://ams.confex.com/ams/11AR11CP/techprogram/paper_42757.htm

Schaaf, C. B., Gao, F., Strahler, A. H., Lucht, W., Li, X., Tsang, T., et al. (2002). First operational BRDF, albedo nadir reflectance products from MODIS. *Remote Sensing of Environment*, *83*(1–2), 135–148. https://doi.org/10.1016/S0034-4257(02)00091-3

Sherman, J. P., & McComiskey, A. (2018). Measurement-based climatology of aerosol direct radiative effect, its sensitivities, and uncertainties from a background southeast US site. *Atmospheric Chemistry and Physics*, *18*(6), 4131–4152. https://doi.org/10.5194/acp-18-4131-2018

Shupe, M. D., Turner, D. D., Zwink, A., Thieman, M. M., Mlawer, E. J., Shippert, T. (2015). Deriving Arctic cloud microphysics at Barrow, Alaska: Algorithms, results, and radiative closure. *Journal of Applied Meteorology and Climatology*, *54*(7), 1675–1689. https://doi.org/10.1175/jamc-d-15-0054.1

Thorsen, T. J., Ferrare, R. A., Hostetler, C. A., Vaughan, M. A., & Fu, Q. (2017). The impact of lidar detection sensitivity on assessing aerosol direct radiative effects. *Geophysical Research Letters*, *44*(17), 9059–9067. https://doi.org/10.1002/2017gl074521

Thorsen, T. J., Ferrare, R. A., Kato, S., & Winker, D. M. (2020). Aerosol direct radiative effect sensitivity analysis. *Journal of Climate*, *33*(14), 6119–6139. https://doi.org/10.1175/jcli-d-19-0669.1

Thorsen, T. J., & Fu, Q. (2015a). Automated retrieval of cloud and aerosol properties from the ARM Raman lidar. Part II: Extinction. *Journal of Atmospheric and Oceanic Technology*, *32*(11), 1999–2023. https://doi.org/10.1175/jtech-d-14-00178.1

Thorsen, T. J., & Fu, Q. (2015b). CALIPSO-inferred aerosol direct radiative effects: Bias estimates using ground-based Raman lidars. *Journal of Geophysical Research: Atmospheres*, *120*(23), 12209–12220. https://doi.org/10.1002/2015jd024095

Thorsen, T. J., Fu, Q., & Comstock, J. M. (2013). Cloud effects on radiative heating rate profiles over Darwin using ARM and A-train radar/lidar observations. *Journal of Geophysical Research: Atmospheres*, *118*(11), 5637–5654. https://doi.org/10.1002/jgrd.50476

Thorsen, T. J., Fu, Q., Newsom, R. K., Turner, D. D., & Comstock, J. M. (2015). Automated retrieval of cloud and aerosol properties from the ARM Raman lidar. Part I: Feature detection. *Journal of Atmospheric and Oceanic Technology*, *32*(11), 1977–1998. https://doi.org/10.1175/jtech-d-14-00150.1

Thorsen, T. J., Winker, D. M., & Ferrare, R. A. (2021). Uncertainty in observational estimates of the aerosol direct radiative effect and forcing. *Journal of Climate*, *34*(1), 195–214. https://doi.org/10.1175/JCLI-D-19-1009.1

Turner, D. D., Vogelmann, A. M., Austin, R. T., Barnard, J. C., Cady-Pereira, K., Chiu, J. C., et al. (2007). *Thin liquid water clouds: Their importance and our challenge* (Vol. 88). American Meteorological Society.

Wood, R. (2005). Drizzle in stratiform boundary layer clouds. Part II: Microphysical aspects. *Journal of the Atmospheric Sciences*, *62*(9), 3034–3050. https://doi.org/10.1175/jas3530.1

Wu, X., Balmes, K. A., & Fu, Q. (2021). Aerosol direct radiative effects at the ARM SGP and TWP sites: Clear Skies. *Journal of Geophysical Research: Atmospheres*, *126*(5), e2020JD033663. https://doi.org/10.1029/2020jd033663

Xia, X., Che, H., Zhu, J., Chen, H., Cong, Z., Deng, X., et al. (2016). Ground-based remote sensing of aerosol climatology in China: Aerosol optical properties, direct radiative effect and its parameterization. *Atmospheric Environment*, *124*, 243–251. https://doi.org/10.1016/j.atmosenv.2015.05.071

Yu, H., Dickinson, R. E., Chin, M., Kaufman, Y. J., Zhou, M., Zhou, L., et al. (2004). Direct radiative effect of aerosols as determined from a combination of MODIS retrievals and GOCART simulations. *Journal of Geophysical Research*, *109*, D03206. https://doi.org/10.1029/2003jd003914

Yu, H., Kaufman, Y. J., Chin, M., Feingold, G., Remer, L. A., Anderson, T. L., et al. (2006). A review of measurement-based assessments of the aerosol direct radiative effect and forcing. *Atmospheric Chemistry and Physics*, *6*(3), 613–666. https://doi.org/10.5194/acp-6-613-2006

Zhao, C., Xie, S., Klein, S. A., Protat, A., Shupe, M. D., McFarlane, S. A., et al. (2012). Toward understanding of differences in current cloud retrievals of ARM ground-based measurements. *Journal of Geophysical Research: Atmospheres*, *117*, D10206. https://doi.org/10.1029/2011JD016792